Study of halo structure of ^{16}C from reaction cross section measurement

T. Zheng [a,b,c], T. Yamaguchi [a], A. Ozawa [a], M. Chiba [a], R. Kanungo [a],
T. Kato [a], K. Katori [a], K. Morimoto [a], T. Ohnishi [a], T. Suda [a],
I. Tanihata [a], Y. Yamaguchi [a], A. Yoshida [a], K. Yoshida [a], H. Toki [a,d],
N. Nakajima [d]

[a] *The Institute of Physical and Chemical Research (RIKEN), Wako, Saitama 351-0198, Japan*
[b] *Department of Physics, Tokyo University of Science, Noda, Chiba 278-8510, Japan*
[c] *Department of Technical Physics, Peking University, Beijing 100871, PR China*
[d] *Research Center for Nuclear Physics (RCNP), Osaka university, Osaka 567-0047, Japan*

Received 4 June 2002; accepted 28 June 2002

Abstract

The reaction cross sections for ^{12,16}C have been measured at the energy of 83 A MeV by a new experimental method. The larger enhancement of the ^{16}C reaction cross section at the low energy has been used to study the density distribution of ^{16}C. The finite-range Glauber-model calculations for different density distributions have been compared with the experimental data. The analysis suggests that ^{16}C mainly has a ^{14}C(core) + 2n structure and shows a strong contribution of $(2s_{1/2})^2$ for valence neutrons. A large extension of the neutron density distribution to a distance far from the center of the nucleus suggests the formation of neutron halo in the ^{16}C nucleus.
© 2002 Elsevier Science B.V. All rights reserved.

1. Introduction

With the development of the radioactive ion-beam technique, it has become possible to extend studies of nuclei far from the stability line. After pioneering work at LBL [1], the interaction cross sections (σ_I) and reaction cross sections (σ_R) for light nuclei were

extensively measured at radioactive nuclear beam facilities at GSI [2], GANIL [3], MSU [4], RIKEN [5] and IMP [6]. The existence of the halo structure in some neutron-rich nuclei, e.g., ^{6}He, ^{11}Li, ^{11}Be, ^{14}Be, ^{19}C, was observed. Among these halo nuclei, ^{11}Be and ^{19}C are considered to be one-neutron (1n)-halo nuclei, and ^{6}He, ^{11}Li and ^{14}Be are two-neutron (2n)-halo nuclei.

Recently the σ_I for carbon isotopes at energy $\sim$960 A MeV were reported [2]. The σ_I of $^AC+^{12}C$ can be compared with the interaction radius (R_I) [1] by

$$\sigma_I = \pi \big[R_I\big(^{12}C\big) + r_0 A^{1/3} \big]^2, \tag{1}$$

where $R_I(^{12}C)$ is the interaction radius of ^{12}C (2.61 fm [1]), and r_0 is selected to reproduce the interaction cross section for ^{12}C. From a comparison between the calculated values by Eq. (1) and the measured values (Fig. 3 in Ref. [2]), it was found that the interaction radii of the carbon isotopes increase faster than this $A^{1/3}$ line for ^{15}C and ^{16}C. This phenomenon suggests an anomalous structure in these neutron-rich carbon isotopes. The interaction cross section of ^{15}C exhibits a large increase from that of ^{14}C. The one neutron separation energy of ^{15}C is 1.218 MeV [7]. It is considered to be a candidate for a one-neutron halo [2]. Measurements of reaction cross sections at low energy [6] and a study concerning one-neutron removal reactions on neutron-rich nuclei [8] support this conjecture. The larger increase in the interaction cross section of ^{16}C from ^{15}C than that of ^{15}C from ^{14}C also suggests the possible existence of a halo structure in the ^{16}C nucleus.

The configuration of ^{16}C has been studied based on its neighbors in the nuclear chart. The main configuration of ^{14}C is considered to be $\pi(1s_{1/2})^2(1p_{3/2})^4$; $\nu(1s_{1/2})^2(1p_{3/2})^4(1p_{1/2})^2$ based on a simple shell model; the spin-parity of the ground state is 0^+. A high excitation energy (6 MeV) of the first excited state support the strong closure of the shell. The spin-parity of the ground state of ^{15}C is $1/2^+$ [9]. The last valence neutron is irregularly assigned to the $2s_{1/2}$ orbital. The spin-parity of the ground state of ^{17}C is $3/2^+$, and the neutron configurations of types $\nu(d_{5/2})^3$ and $\nu(d_{5/2})^2(s_{1/2})$ share almost equal strengths [10]. Because the spin-parity of ^{16}C is 0^+, both the $\nu(2s_{1/2})^2$ and $\nu(1d_{5/2})^2$ neutron configurations can therefore be contributed.

Compared with the known 2n-halo nuclei, studying ^{16}C has its own significance. It is a candidate 2n-halo nucleus, which is closer to the stability line than other 2n-halo nuclei. Other 2n-halo nuclei (^{6}He, ^{11}Li and ^{14}Be) are three-body systems (core $+$ n $+$ n) in which the two-body subsystems are unbound, the so-called Borromean systems. If ^{16}C can also be treated as a core $+$ n $+$ n three-body system, it is not a Borromean system because the two-body subsystems $^{14}C + n$ are bound as ^{15}C. It thus provides a tool to study the correlation between the valence neutrons by measuring the momentum distribution and the neutron-removal cross sections. For ^{16}C, the one-neutron (S_n) separation energy is 4.250 MeV, and the two-neutron (S_{2n}) separation energy is 5.468 MeV [7]. This shows that pairing of the last two valence neutrons plays a very important role in ^{16}C. The two-neutron separation energy is much larger than that of other known 2n-halo nuclei [2], and is thus very helpful to study whether a halo structure is formed or not.

In the present experiment, a new method was used to measure the reaction cross section of ^{16}C. In this new method, the time-of-flight (TOF), the energy loss (ΔE) and total energy (E) were measured after the reaction target. By adding the TOF, the reactions that occurred in the target and in the detectors were separated well.

A finite-range Glauber-model calculation was introduced to study the density distribution and the neutron configuration of ^{16}C. The range parameter of nucleus–nucleus interactions was determined from the measured ^{12}C+^{12}C reaction cross section. The halo structure of ^{16}C has been seen and $(2s_{1/2})^2$ has been suggested to be the main configuration of the last two neutrons.

2. Experiment and analysis

The reaction cross section (σ_R) for ^{16}C at the intermediate energy was measured by a new transmission method. The experiment was performed at the RIken Projectile fragment Separator (RIPS) [11] in the RIKEN Ring Cyclotron Facility. Secondary ^{12,16}C beams were produced via the projectile fragmentation of a ^{22}Ne primary beam that was accelerated to ~110 A MeV by the RIKEN Ring Cyclotron (RRC). The beryllium production targets of 2 and 4 mm in thickness were used. The experimental setup is shown in Fig. 1.

At the first dispersive focus in RIPS (F1), a PPAC (Parallel Plate Avalanche Counter) was used to monitor the beam size and to obtain the momenta of secondary nuclei (the momentum dispersion at F1 was 2.4 cm/%). A wedge-shaped degrader (WD) with a central thickness of 1098 mg/cm^2 was placed just before the PPAC. At the second focus (F2), two PPACs were placed so as to define the incident angel and position of the beam. Two silicon detectors (150 μm × 2) were used to measure the energy loss of the incident nucleus. An ultra-fast timing scintillator with an intrinsic time resolution of 30 ps in σ [12] was used to obtain the start signal for a TOF measurement. From F1 to F2, the beam was
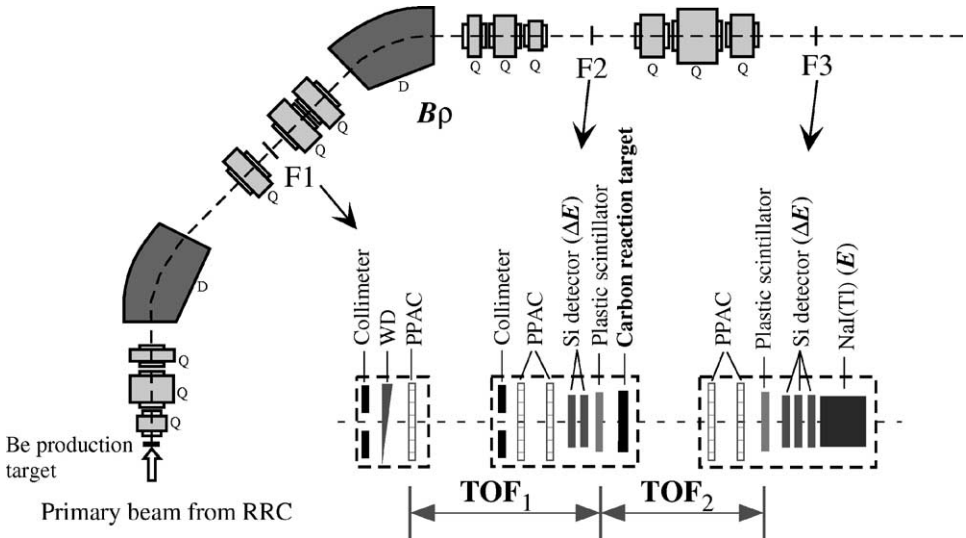

Fig. 1. Schematic view of the experimental setup at fragment separator RIPS. F1–F3 denote the three foci. Q denotes the quadrupole magnet and D denotes the dipole magnet. The measured quantities ($B\rho$, ΔE, TOF and E) are shown by bold characters.

bent 45° by a dipole magnet. The position information at F1 together with the magnetic field of the dipole magnet gave the magnetic rigidity ($B\rho$) of the fragments. Before the reaction target, the ^{16}C was identified and isolated from the other nuclei by the $B\rho-\Delta E-$TOF method. The reaction target was a carbon plate of 370 mg/cm^2 in thickness. The ^{16}C beam energy was 83 A MeV in the middle of the reaction target, while the incident energy was 86 A MeV and the outgoing energy was 80 A MeV.

After the reaction target, the particles were identified by a new method for the reaction-cross-section measurement. In addition to the usual $\Delta E-E$ measurement, the present method also measured the TOF between the reaction target and the detector. The particles going out from the target flew a distance of ∼6 m. A quadrupole triplet was used to transport the beam. The transmission efficiency was carefully checked during both the measurement and an offline analysis. After putting a restriction on the emittance of the incident particles, the beam size on the second PPAC at F2 was 20 × 5 mm^2 and incident angle was less than ±20 mrad, the transmission became constant. At the third focus (F3), two PPACs were used to monitor the beam size and the transmission from F2 to F3. An ultra-fast timing scintillator gave the stop signal for a TOF measurement. To eliminate the channeling effect on Z-identification, three silicon detectors (150 μm × 3) were used to measure the energy loss (ΔE). The total energy (E) was measured by a NaI(Tl) detector (∅3″, 6 cm thickness, energy resolution of 0.7% in FWHM for 110 A MeV ^{22}Ne) [13]. The NaI(Tl) detector was surrounded by a set of plastic counters, which were used to detect the emitted charged-particles or neutrons from reactions in the NaI(Tl) detector. The particle identification was based on the TOF–$\Delta E-E$ method. This method overcomes the shortcomings of the usual $\Delta E-E$ method by which it is difficult to separate those reactions in the target and those in the detectors. By the present experimental system, the reactions that occurred at different places were well separated because they gave different TOF. Fig. 2(a) shows the charge (Z) identification and Fig. 2(b) shows the mass (A) identification after selecting only carbon isotopes. Using the relation $E \times T^2 \propto A$, the mass spectrum of the carbon isotopes was obtained, as shown in Fig. 3, where T is the time of flight.

Measurements were performed with and without a reaction target. The number of incident particles (N_1) was determined by the $B\rho-\Delta E$–TOF method. The background of the ^{16}C was estimated to be very small ($<10^{-4}$), which was negligible for determining the reaction cross section. The number of outgoing ^{16}C particles without any change in the target (N_2) was determined by the TOF–$\Delta E-E$ method. By using the ratios of these two numbers ($R = N_2/N_1$), the reaction cross section of ^{16}C+^{12}C was determined by

$$\sigma_R = -\frac{1}{t} \ln\left(\frac{R_i}{R_o}\right),\qquad(2)$$

where t is the thickness (atom/cm^2) of the reaction target, R_i denotes the ratio in the measurement with the target and R_o denotes the ratio in the measurement without the target. In order to obtain the reaction cross section (σ_R) of ^{16}C, the number of the inelastically scattered ^{16}C were subtracted from the total number of ^{16}C. The method used to subtract the inelastic ^{16}C is shown in Fig. 4, where only the ^{16}C events were selected from the mass spectrum (shown in Fig. 3). Firstly, the events with T larger
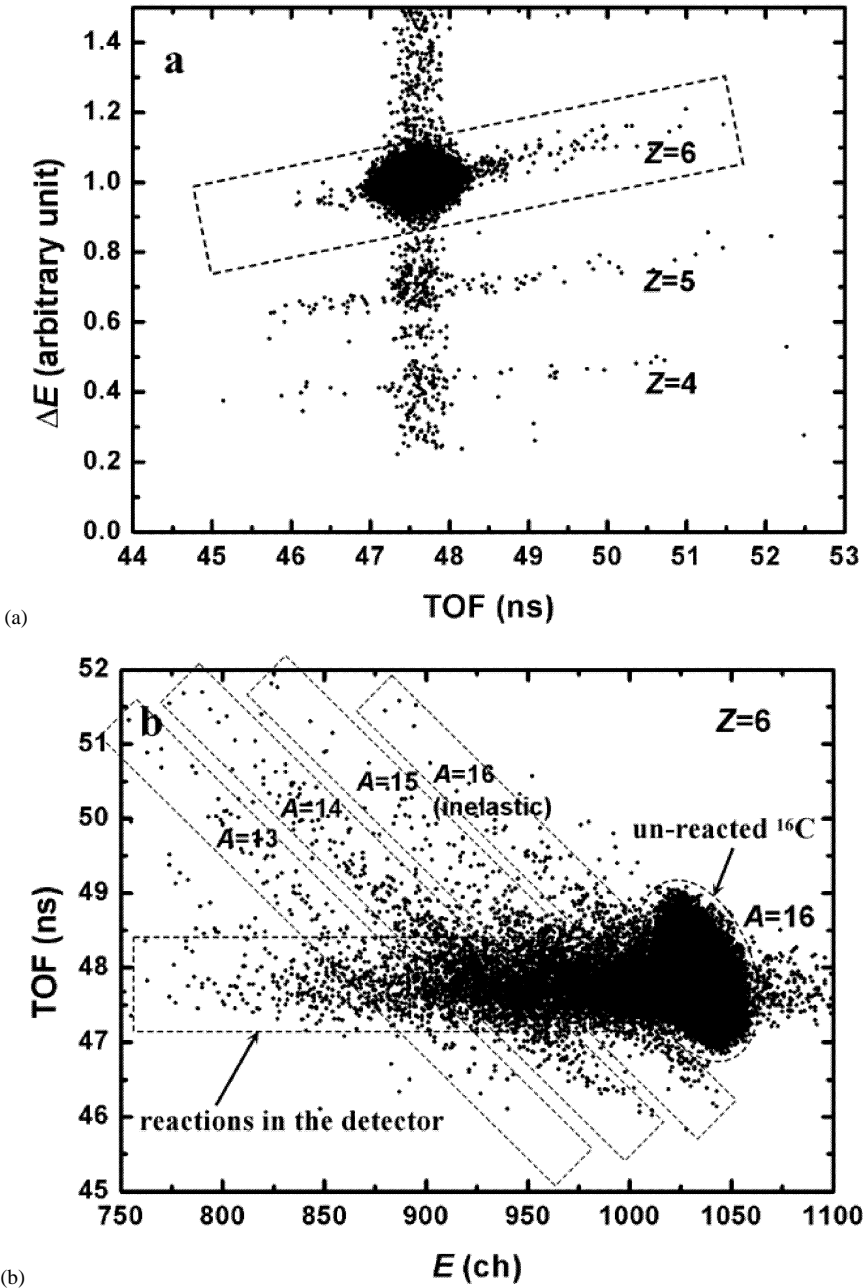
(a)

(b)

Fig. 2. Charge (a) and mass (b) identification by the TOF–ΔE–E method. In (a), the $Z = 6$ events are selected. In (b), carbon isotopes of different mass are separated. The long tail with a constant TOF ($\sim$47.2–48.4 ns) extending from high energy to low energy is due to reactions in the NaI (Tl) detector. The branches extending up and down were particles produced in the reaction target.
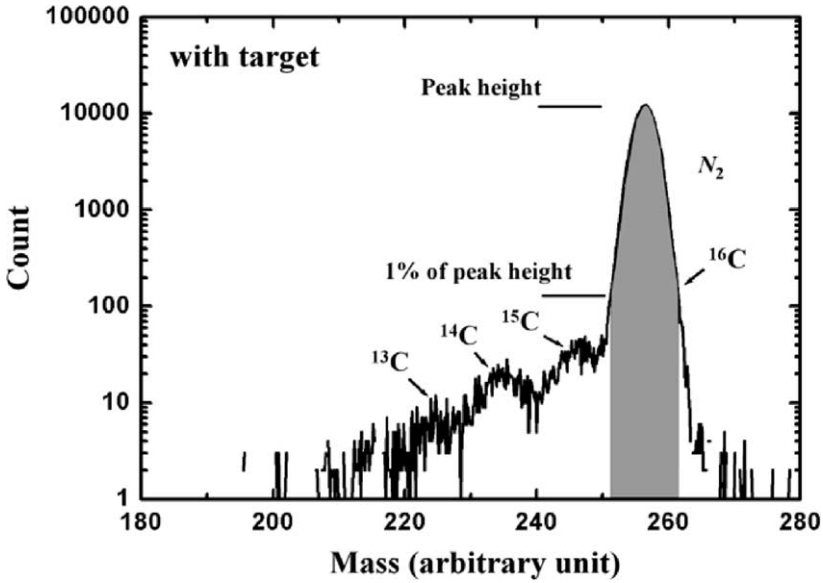
Fig. 3. Mass spectrum of selected carbon isotopes in a measurement with the Carbon target. The number (N_2) of ^{16}C is determined from the shaded area.
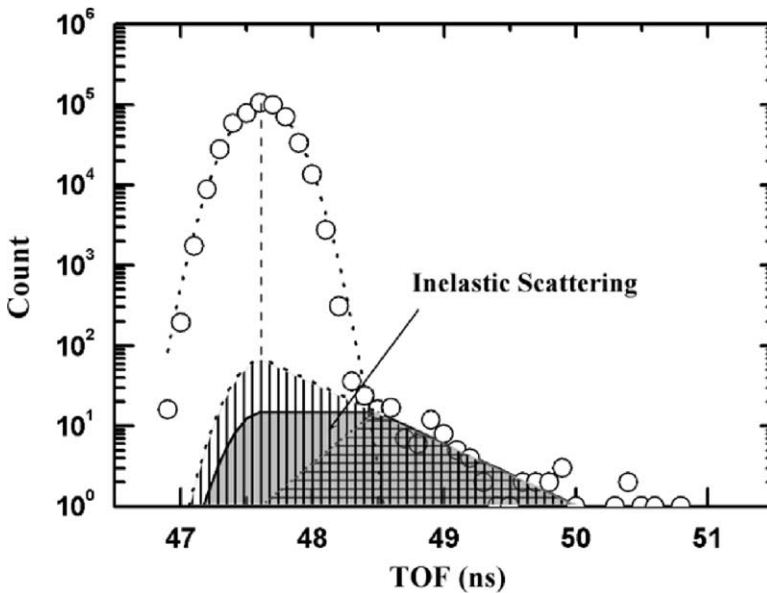

Fig. 4. Method for determining inelastic ^{16}C events. The main peak was fitted by a Gaussian function and subtracted from the spectrum. The inelastic part was fitted by an exponential curve. The shaded area gives the count of the inelastic scattering event. The area marked by the horizontal line gives the lower estimation of the inelastic scattering. The area marked by the vertical line gives the upper estimation of the inelastic scattering. The TOF resolution was taken in to account in the estimation.

Table 1
The reaction cross sections of ^{16}C

E (A MeV)	σ_R (mb)
83	1237 ± 25 (present measurement)
960	1036 ± 11 [2][*]
39	1559 ± 44 [6]

[*] Interaction cross section σ_I.

Table 2
The reaction cross sections of ^{12}C

E (A MeV)	σ_R (mb)	E (A MeV)	σ_R (mb)
83	957 ± 39 (present measurement)	200	864 ± 45 [14]
30	1316 ± 40 [14]	250	873 ± 60 [14]
41	1173 ± 56 [6]	300	858 ± 60 [14]
83	965 ± 30 [14]	790	856 ± 9 [2][*]
		950	853 ± 6 [2][*]

[*] Interaction cross section σ_I.

than 48.5 ns can be considered to come from inelastic scattering in the target. Under the main peak of the TOF, although there were mainly the un-reacted ^{16}C, the inelastic scattering events of ^{16}C were also included as well. Those events should be excluded from the number of un-reacted events in order to obtain the reaction cross section. Due to the resolution of TOF and E, it was impossible to separate those inelastic scattering events embedded in the main peak. It was estimated by the following method. The main peak was fitted by a Gaussian function. After subtracting the Gaussian part from the spectrum, the inelastic part was fitted by an exponential curve, as shown by solid line in Fig. 4. The number of inelastic events under this Gaussian peak was estimated under three different conditions. The first was to assume that the background under the main peak to be constant to the center of the peak and the Gaussian tail to include the resolution of the TOF. Thus-obtained shaded area was used as the central value of the count of the inelastic scattering events. The second was to assume the inelastic scattering to be zero at the center of the main peak. This area, marked by horizontal lines, was used as the lower limit of the inelastic scattering. The third was to assume a exponential increase of the inelastic scattering below the main peak. This area, marked by vertical lines, was used as the upper limit of the inelastic scattering. Because the estimated inelastic process was <1% of the total reaction events (∼26 mb, central value), the uncertainty had an extremely small effect on the σ_R. The determined reaction cross sections of ^{16}C are summarized in Table 1.

The reaction cross section for $^{12}C+^{12}C$ at 83 A MeV was obtained by the same method. The reaction cross sections of ^{12}C are summarized in Table 2. The present measurement agrees well with a previous measurement [14] at the same energy. The agreement proves that this new method is valid for measuring the reaction cross section.

3. Discussion of the results

The experimental results were firstly compared with a phenomenological parameterization for the reaction cross section by S. Kox et al. [14],

$$\sigma_R(E) = \pi r_0^2 \left[A_P^{1/3} + A_T^{1/3} + a \frac{A_P^{1/3} A_T^{1/3}}{A_P^{1/3} + A_T^{1/3}} - c(E) \right]^2 \left(1 - \frac{B_c}{E_{cm}} \right), \tag{3}$$

where B_c is the Coulomb barrier, E_{cm} is the center-of-mass energy and $c(E)$ is an energy-dependent surface transparency parameter the parameter r_0 is 1.1 fm and a is 1.85.

Although it reproduces the energy dependence of the reaction cross section for the $^{12}C+^{12}C$ reaction very well, deviations have been observed at both high and low energy for the $^{16}C+^{12}C$ reaction, as shown in Fig. 5. It can be seen that the measured reaction cross sections at low energy (below 100 A MeV) have a much larger enhancement than that at 960 A MeV. This enhancement suggests the existence of a low-density tail at a large distance from the center of the ^{16}C nucleus.

By using the Glauber model [15], under the optical-limit approximation [16], after including a Coulomb correction [14], the reaction cross section was calculated by

$$\sigma_R = 2\pi \int [1 - T(b)] b \, db \left(1 - \frac{B_c}{E_{cm}} \right), \tag{4}$$

where $T(b)$ is the transmission at an impact parameter of b. $T(b)$ is determined by the density overlap of the projectile and target, and by the total nucleon–nucleon (NN) cross section.
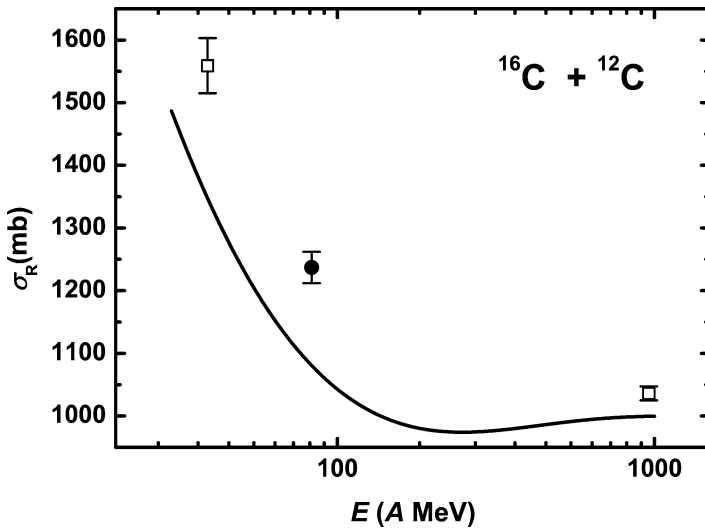

Fig. 5. Reaction cross section for $^{16}C+^{12}C$ and a comparison with a phenomenological parameterization (Eq. (3)). The filled circle denotes the present measurement and the open squares are the previous measurement.

Under the zero-range limit approximation [16], $T(b)$ is written as

$$T(b) = \exp\left\{-\sum_{ij} \sigma_{ij} \int\int_P \rho^z_{Pi}(s)\rho^z_{Tj}(b+s)\, ds\right\}, \tag{5}$$

where P denotes the projectile and T denotes the target; i, j are used to distinguish a proton and a neutron. $\rho^z_{Ki}(s)$ is a z-direction integrated nucleon-density distribution,

$$\rho^z_{Ki}(s) = \int_{-\infty}^{\infty} \rho_{Ki}\left(\sqrt{s^2+z^2}\right) dz, \tag{6}$$

where K denotes P or T. This is the so-called zero-range Glauber-model calculation. It was widely used in various analyses ([1,5,17,18]), and was proved to work well in the high-energy region. However, in the low-energy region, it always underestimates the reaction cross section [17]. In Ref. [17], the authors state that the differences between the data and calculated values vary from nucleus to nucleus. A difference factor was introduced for quantitative considerations. The difference factor is defined as

$$d = \frac{\sigma_R(\text{Exp}) - \sigma_R(\text{Gla})}{\sigma_R(\text{Gla})}$$

from the σ_R of stable nuclei. In Ref. [18], a calculation for the intermediate-energy region was done by multiplying an enhancement factor, which was determined phenomenologically from the data of a stable nucleus. The σ_R of an unstable nucleus was assumed to have the same factor if it had the normal density distribution. An estimation of a change in the density distribution was made based on the deviation of σ_R from the corrected value. However it is not clear that we can apply the same difference factor for different nuclei.

In a present discussion, we introduce the finite-range Glauber-model. In the finite-range formalism, the profile function is parameterized in the form [16]

$$\Gamma_{ij}(b_{\text{eff}}) = \frac{1 - i\alpha}{4\pi\beta_{ij}^2}\sigma_{ij}\exp\left(-\frac{b_{\text{eff}}^2}{2\beta_{ij}^2}\right), \tag{7}$$

where b_{eff} is the impact parameter between two colliding nucleons, β is the range parameter, which determines the fall-off of the angular distribution of the NN elastic scattering. In the optical-limit approximation, α does not contribute to σ_R.

The reaction cross section is calculated by using Eq. (4), with the transmission in the form of

$$T(b) = \exp\left\{-\int\int_P \int\int_T \sum_{ij}\left[\Gamma_{ij}(b+s-t)\rho^z_{Ti}(t)\rho^z_{Pj}(s)\right] ds\, dt\right\}. \tag{8}$$

In the finite-range Glauber-model calculation, it is very important to determine the range parameter (β_{ij}) in the profile function (Eq. (7)).

For light stable nuclei, the shell-model Harmonic-Oscillator (HO)-type density [19], which includes the contributions up to the sd-shell, is a good approximation for the density. For ^{12}C, we used the HO-type density distribution that reproduces the interaction cross section at high energy [2]. The size parameter is $a = 1.571$ fm. The range parameters

(β_{ij}) are assumed to depend on the energy smoothly, and are same for all combinations of i and j. The range parameters (β_{ij}) are obtained by fitting the $^{12}C+^{12}C$ reaction cross sections from 30 A MeV to 1 A GeV, as

$$\beta_{NN} = 0.996 \exp\left(-\frac{E}{106.679}\right) + 0.089. \tag{9}$$

The result is shown in Fig. 6. The previous range parameter values of β_{pp} and β_{pn} [20], determined from proton–nucleus scattering, are also shown in the figure. Although the energy dependences are similar, we can see systematic differences between the present and published values. The reason is not clear at this moment. For the present purpose, we used a range parameter obtained by Eq. (9) as an effective range parameter, assuming that the effective range parameter does not depend on the nuclides. We applied this parameter for normal neutron-rich nucleus ^{14}C. The energy dependence of the $^{14}C+^{12}C$ reaction cross sections were fitted well, as shown in Fig. 7.

Assuming that the density distribution of ^{16}C is also a HO-type, and determining the size parameter ($a = 1.778$ fm) by fitting the measured interaction cross section at high energy [2], the results of the Glauber-model calculations are shown in Fig. 8. At low energy, the zero-range Glauber-model calculation underestimates the reaction cross section, as expected. Compared with the zero-range Glauber-model calculation, the agreement of the finite-range Glauber-model calculation with the experimental results is greatly improved. However, the finite-range calculation still underestimates σ_R at lower energy. It clearly shows that the reaction cross sections of ^{16}C at lower energy increase much more than those of ^{12}C and ^{14}C. It thus suggests a longer tail in the ^{16}C density distribution.

For a halo nucleus, a core + halo model is widely used [21]. Based on the assumption that ^{16}C is a three-body system composed of a core (^{14}C) and two valence neutrons, the possible halo structure of ^{16}C is studied. A HO-type density distribution that fits the
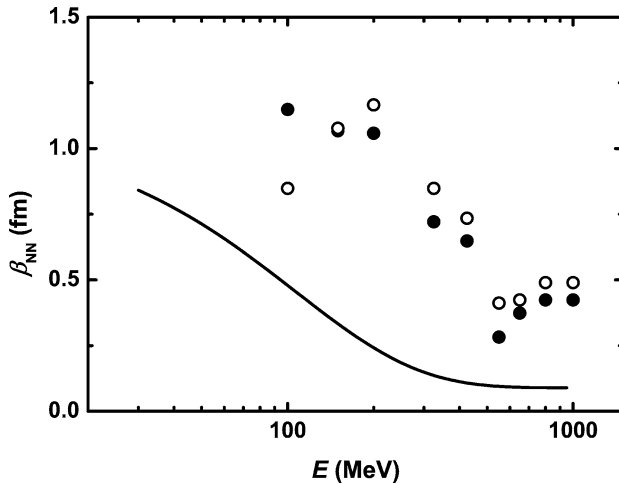

Fig. 6. Effective range parameter obtained from the best fitting to the measured reaction cross section for $^{12}C+^{12}C$. The scattered plots show the published range parameter, where open circles and filled circles denote those of the proton–neutron (pn) and proton–proton (pp), respectively.
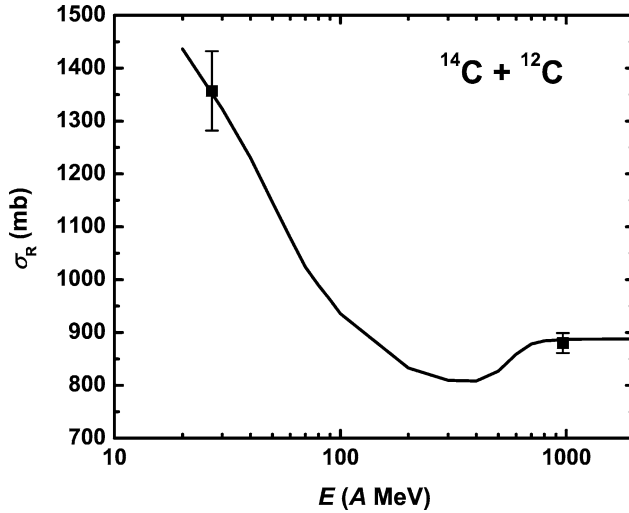
Fig. 7. The finite-range Glauber-model calculation for ^{14}C+^{12}C using the effective range parameter. The density of ^{14}C is HO-type with a size parameter of $a = 1.547$ fm.
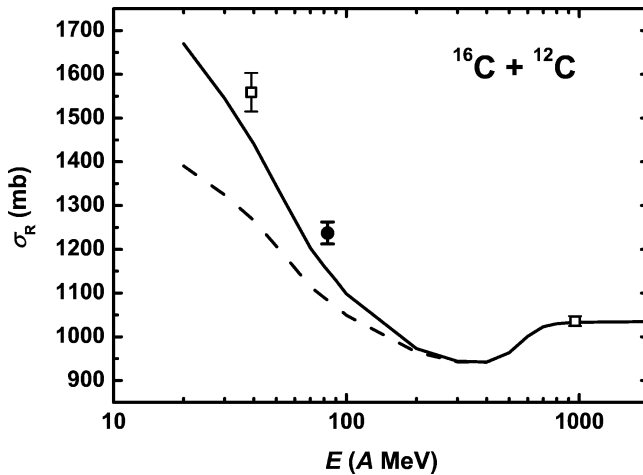

Fig. 8. The Glauber-model calculation for ^{16}C+^{12}C. The density of ^{16}C is the HO-type with a size parameter of $a = 1.778$ fm. The target was ^{12}C with a size parameter of $a = 1.571$ fm. The scatter plots are measured value and denotations are same as those in Fig. 5. A solid line shows the finite-range calculation and a dashed line shows the zero-range calculation.

^{14}C+^{12}C cross section at both high and low energy is used for the core ^{14}C. For the valence neutrons, two possible configurations were assumed, $\nu(2s_{1/2})^2$ or $\nu(1d_{5/2})^2$. The wave function of the valence neutron was obtained by solving the eigenvalue problem of the Schrödinger equation in the Woods–Saxon (WS) and Coulomb potential. The calculation was performed using the code WAVEFUNC [22]. In this code, the wave function of a
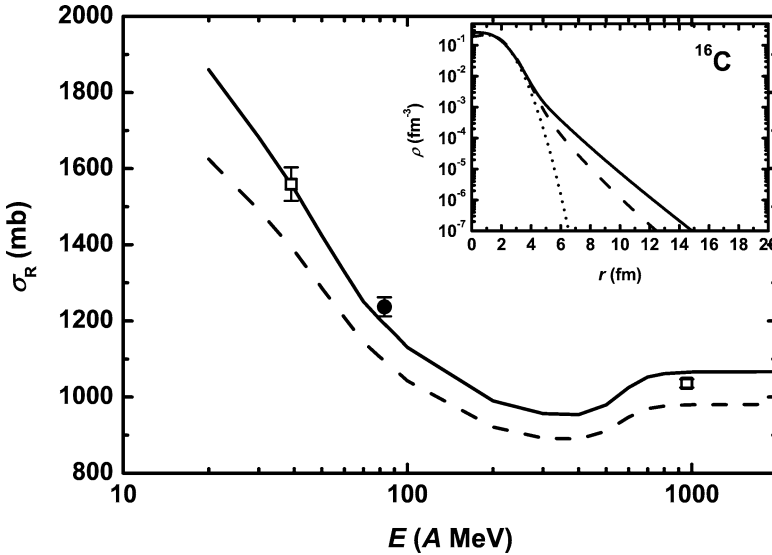
Fig. 9. Finite-range Glauber calculation for $^{16}C+^{12}C$ while the density distribution of ^{16}C was obtained by a core + halo model. The solid line shows a calculation using a density of core + $(2s_{1/2})^2$; and the dashed line shows a calculation using a density of core + $(1d_{5/2})^2$. The densities are shown in the inset using the same denotations. The density of the core (^{14}C) is of the HO-type with a size parameter of $a = 1.547$ fm, shown by a dotted line. The target was ^{12}C with a size parameter of $a = 1.571$ fm.

neutron in the s or d orbital was calculated in a ^{14}C potential, where the depth of the potential was adjusted so as to reproduce the single-nucleon separation energy. The single-neutron separation energy was taken to be half of the 2n separation energy of ^{16}C ($S_{2n}/2$), that is 2.734 MeV. From the wave function of the valence neutron, the density distribution was obtained. Neglecting the correlations between the two neutrons, the density of the two valence neutrons was added to the density of the core (^{14}C) to obtain the density distribution of ^{16}C. The results of the finite-range Glauber-model calculation for ^{16}C are shown in Fig. 9.

The finite-range calculation for $\nu(2s_{1/2})^2$ configuration agrees well with the experimental data much better than that of the $\nu(1d_{5/2})^2$ configuration. It therefore shows that $\nu(2s_{1/2})^2$ is the dominant component of the halo. Although it is a small amount, the deviation from the experimental data remains under this calculation. This is because the slope of the density tail is fixed by the separation energy. In addition, even if the separation energy is changed arbitrarily around the $S_{2n}/2$, the high-energy cross section and the low-energy cross sections cannot be fit simultaneously, and deviation from the experimental data still remains.

Therefore, the density distribution of ^{16}C was studied under less constraint. The assumed density distribution is a HO-type density plus a Yukawa-square tail. At a large distance from the center of the nucleus, this single-particle density asymptotically approaches the Yukawa-square function. It is therefore considered to be a good approximation to the shape of the single-particle density outside the core [18].

For the neutron density distribution of ^{16}C:

$$\rho_n(r) = \frac{0.4014}{a^3}\left(1 + \frac{2r^2}{a^2}\right)\exp\left(-\frac{r^2}{a^2}\right) \quad (r < r_c)$$

$$= \frac{C\exp(-\lambda r)}{r^2} \qquad\qquad (r \geqslant r_c). \tag{10}$$

The proton density distribution was fixed to be

$$\rho_p(r) = \frac{0.4014}{a^3}\left(1 + \frac{4r^2}{3a^2}\right)\exp\left(-\frac{r^2}{a^2}\right) \quad (r < r_c), \tag{11}$$

where a is the size parameter of the HO-type density, r_c the distance from the center of the nucleus where the HO-type density is connected to the Yukawa-square tail, and λ the slope of the Yukawa-square tail. The size parameter a of the HO-density is common for the neutron and the proton. All three parameters a, λ and r_c are free parameters. The density distributions of proton and neutron are normalized to give $Z = 6$ and $N = 10$, respectively. To obtain the effective density of the nucleus, the parameters in the density distribution are adjusted to fit the experimental σ_R at different energies. By the least χ^2 fitting of the measured reaction cross section, all of the parameters can be determined.

We first set the size parameter of the HO-type density to be the same as that of ^{14}C in the ground state, which was obtained by fitting the interaction cross section at high energy, $a = 1.547$ fm. In the inset in Fig. 10, the density distribution of the best fit ($\chi^2 = 2.585$) to the experimental data is shown by the dotted line. The fitting to the σ_R data is shown in Fig. 10 by the dashed line. The fitting to the data is slightly better than that of the core $+ (2s_{1/2})^2$.

Secondly, size parameter of the HO-type density was also set to be free. The obtained density is shown in the inset in Fig. 10 by the solid line. Again it shows that the tail is necessary in order to obtain the best fit ($\chi^2 = 2.539$), which is shown in Fig. 10 by the solid line. The shaded region shows the uncertainty of the determined density. The obtained densities under two assumptions are identical within the error. It therefore indicates that the core ^{14}C is not visibly different from the free ^{14}C.

From the above analysis, it is found that a long, low-density neutron tail is necessary to understand the reaction cross sections of the ^{16}C nucleus. The ^{16}C nucleus is well-described by the ^{14}C $+$ 2n model with a slight modification of the ^{14}C core in ^{16}C. The best-fitted density has a tail slightly longer than the $(2s_{1/2})^2$ tail. This difference may suggest the effect of the correlation between the two valence neutrons. More studies on this correlation are expected.

In Fig. 11, the densities of ^{16}C that were studied in different ways are summarized. The density distribution predicted by the Relativistic Continuum Hartree–Bogoliubov (RCHB) theory [23] is also shown by the dashed curve. Although this theory reproduced the ^{11}Li tail very well, it shows a much shorter tail for ^{16}C.

From the best fit (solid curve in Fig. 10) to the experimental data, the effective density of ^{16}C was obtained, as shown in Fig. 11 by the solid curve. The root-mean-square (rms) matter radius of ^{16}C was deduced from the determined density distribution to be

$$\langle r^2 \rangle^{1/2} = \left(\frac{4\pi \int r^4 \rho(r)\,dr}{4\pi \int r^2 \rho(r)\,dr}\right)^{1/2} = 2.64 \pm 0.05 \text{ fm}. \tag{12}$$
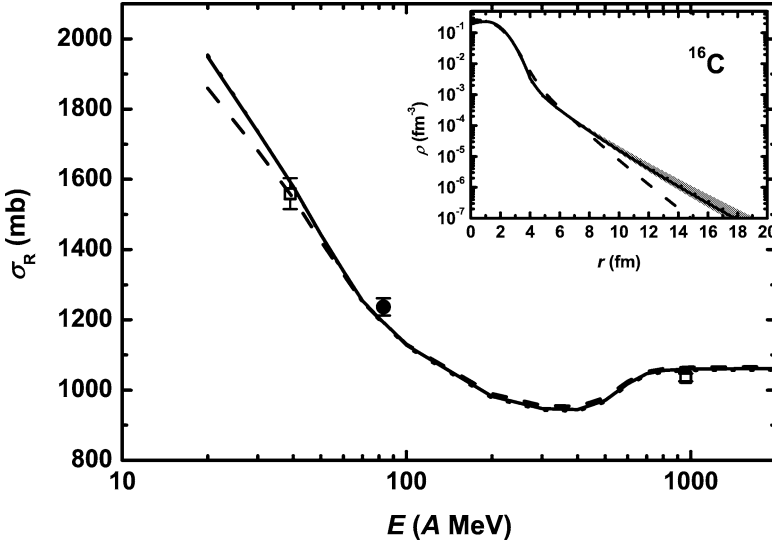
Fig. 10. Finite-range Glauber-model calculation using the HO + Yukawa-square density, while all of the parameters were determined by the best fitting to the experimental data. The solid line shows a calculation using a density with a size parameter of $a = 1.560$ fm, the slope of the Yukawa-square tail is 0.50 fm^{-1}, and the connecting radius is 3.96 fm. The dotted line shows a calculation using a density with a size parameter of $a = 1.547$ fm, the slope of the Yukawa-square tail is 0.48 fm^{-1}, and the connecting radius is 3.96 fm. For comparison, the calculation using a density of core + $(2s_{1/2})^2$ is shown as well by the dashed line. The densities are shown in the small figure using the same denotations. The two HO + Yukawa-square densities are identical within error.
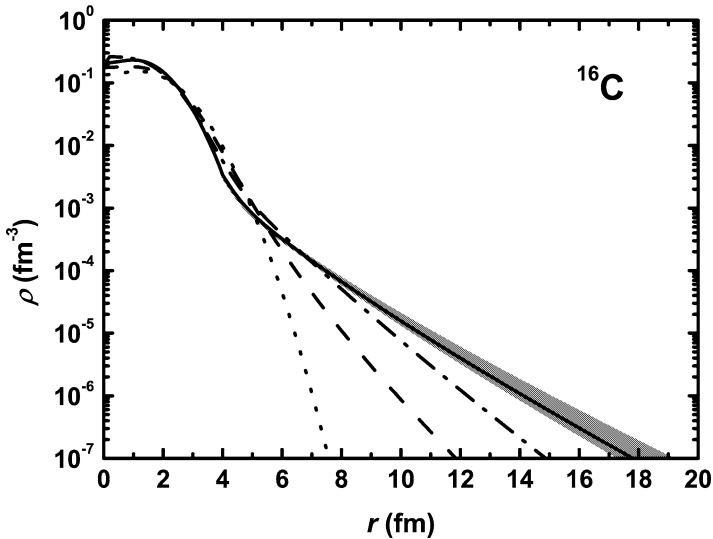

Fig. 11. Comparison of the effective density distribution of ^{16}C (solid line, the shaded area gives the error) with the simple HO-type density (dotted line), core (^{14}C) + $(2s_{1/2})^2$ density (dot-dashed line) and the density from RCHB theoretical prediction (long-dashed line).

This root-mean-square matter radius of ^{16}C is consistent with that obtained from the interaction cross section at high energy, assuming a HO-type density [2], where $\langle r^2 \rangle^{1/2} = 2.70 \pm 0.03$ fm, and with a prediction by RCHB theory [23], where $\langle r^2 \rangle^{1/2} = 2.67$ fm. This shows that $\langle r^2 \rangle^{1/2}$ is determined rather well insensitive from the assumption of the density distribution.

4. Summary

The reaction cross section for ^{16}C at 83 A MeV was measured by a new experimental method. This new method provided a clear separation of the reactions that occurred in the target and in the detectors, and thus provided accurate data.

The finite-range Glauber-model calculation has been introduced. The range parameter was fixed by the $^{12}C+^{12}C$ system and also confirmed to work well in the $^{14}C+^{12}C$ reaction. From a finite-range Glauber-model calculation, in which a core + 2n density distribution was used, the $s_{1/2}$ configuration was found to be dominant. The effective density of ^{16}C was obtained through the χ^2-fitting procedure. The result shows that a longer low-density tail is necessary to reproduce the cross sections with minimal assumptions. This observation suggests the formation of a neutron halo in the ^{16}C nucleus.

Acknowledgements

References

[1] I. Tanihata, H. Hamagaki, O. Hashimoto, S. Nakamiya, Y. Shida, N. Yoshikawa, O. Yamakawa, K. Sugimoto, T. Kobayashi, D.E. Greiner, N. Takahashi, Y. Nojiri, Phys. Lett. B 160 (1985) 380;
I. Tanihata, H. Hamagaki, O. Hashimoto, Y. Shida, N. Yoshikawa, K. Sugimoto, O. Yamakawa, T. Kobayashi, N. Takahashi, Phys. Rev. Lett. 55 (1985) 2676.
[2] A. Ozawa, O. Bochkarev, L. Chulkov, D. Cortina, H. Geissel, M. Hellström, M. Ivanov, R. Janik, K. Kimura, T. Kobayashi, A.A. Korsheninnikov, G. Münzenberg, F. Nickel, Y. Ogawa, A.A. Ogloblin, M. Pfützner, V. Pribora, H. Simon, B. Sitár, P. Strmen, K. Sümmerer, T. Suzuki, I. Tanihata, M. Winkler, K. Yoshida, Nucl. Phys. A 691 (2001) 599, and references therein.
[3] W. Mittig, J.M. Chouvel, W.L. Zhan, L. Bianchi, A. Cunsolo, B. Fernandez, A. Foti, J. Gastebois, A. Gillibert, C. Gregoire, Y. Schutz, C. Stephan, Phys. Rev. Lett. 59 (1987) 1889.
[4] R.E. Warner, J.H. Kelley, P. Zecher, F.D. Becchetti, J.A. Brown, C.L. Carpenter, A. Galonsky, J. Kruse, A. Muthukrishnan, A. Nadasen, R.M. Ronningen, P. Schwandt, B.M. Sherrill, J. Wang, J.S. Winfield, Phys. Rev. C 52 (1995) R1166.
[5] M. Fukuda, T. Ichihara, N. Inabe, T. Kubo, H. Kumagai, T. Nakagawa, Y. Yano, I. Tanihata, M. Adachi, K. Asahi, M. Kouguchi, M. Ishihara, H. Sagawa, S. Shimoura, Phys. Lett. B 268 (1991) 339.
[6] D.Q. Fang, W.Q. Shen, J. Feng, X.Z. Cai, J.S. Wang, Q.M. Su, H.Y. Zhang, P.Y. Hu, Y.G. Ma, Y.T. Zhu, S.L. Li, H.Y. Wu, Q.B. Gou, G.M. Jin, W.L. Zhan, Z.Y. Guo, G.Q. Xiao, Phys. Rev. C 61 (2000) 064311.
[7] G. Audi, O. Bersillon, J. Blachot, A.H. Wapstra, Nucl. Phys. A 624 (1997) 1.

 [8] E. Sauvan, F. Carstoiu, N.A. Orr, J.C. Angélique, W.N. Catford, N.M. Clarke, M. Mac Cormick, N. Curtis, M. Freer, S. Grévy, C. Le Brun, M. Lewitowicz, E. Liégard, F.M. Marqués, P. Roussel-Chomaz, M.G. Saint Laurent, M. Shawcross, J.S. Winfield, Phys. Lett. B 491 (2000) 1.

 [9] J.D. Goss, A.A. Rollefson, C.P. Browne, R.A. Blue, H.R. Weller, Phys. Rev. C 8 (1973) 514.

[10] K. Asahi, H. Ogawa, H. Ueno, D. Kameda, H. Miyoshi, Y. Kobayashi, A. Yoshimi, K. Yogo, A. Goto, T. Suga, K. Sakai, N. Imai, Y.X. Watanabe, K. Yoneda, N. Fukuda, N. Aoi, A. Yoshido, T. Kubo, M. Ishihara, W.-D. Schmidt-Ott, G. Neyens, S. Teughels, RIKEN Review 39 (2001) 142.

[11] T. Kubo, M. Ishihara, N. Inabe, H. Kumagai, I. Tanihata, K. Yoshida, Nucl. Instrum. Methods B 70 (1992) 309.

[12] R. Kanungo, M. Chiba, N. Iwasa, S. Nishimura, A. Ozawa, C. Samanta, T. Suda, T. Suzuki, T. Yamaguchi, T. Zheng, I. Tanihata, Phys. Rev. Lett. 88 (2002) 142502.

[13] T. Suda, M. Chiba, T. Izumikawa, R. Kanungo, T. Kato, A. Ozawa, T. Suzuki, I. Tanihata, T. Yamaguchi, T. Zheng, RIKEN Accel. Prog. Rep. 35 (2002) 42.

[14] S. Kox, A. Gamp, C. Perrin, J. Arvieux, R. Bertholet, J.F. Bruandet, M. Buenerd, R. Cherkaoui, A.J. Cole, Y. El-Masri, N. Longequeue, J. Menet, F. Merchez, J.B. Viano, Phys. Rev. C 35 (1987) 1678, and references therein.

[15] R.J. Glauber, in: W.E. Brittin, L.G. Dunham (Eds.), in: Lectures in Theoretical Physics, Vol. 1, Interscience, New York, 1959, p. 315.

[16] Y. Ogawa, K. Yabana, Y. Suzuki, Nucl. Phys. A 543 (1992) 722, and references therein.

[17] A. Ozawa, I. Tanihata, T. Kobayashi, Y. Sugahara, O. Yamakawa, K. Omata, K. Sugimoto, D. Olson, W. Christie, H. Wieman, Nucl. Phys. A 608 (1996) 63.

[18] M. Fukuda, et al., Nucl. Phys. A 656 (1999) 209.

[19] L.R.B. Elton, Nuclear Sizes, Oxford Univ. Press, London, 1961, pp. 21–22.

[20] L. Ray, Phys. Rev. C 20 (1979) 1857.

[21] S. Shimoura, T. Nakamura, H. Okamura, H. Okuno, H. Sakai, M. Ishihara, N. Inabe, T. Kubo, H. Kumagai, T. Nakagawa, I. Tanihata, RIKEN-AF-NP-134.

[22] S. Hirenzaki, WAVEFUNC code, RIKEN (1993).

[23] J. Meng, S.-G. Zhou, I. Tanihata, submitted to Phys. Lett. B;
     J. Meng, Nucl. Phys. A 635 (1998) 3;
     J. Meng, P. Ring, Phys. Rev. Lett. 77 (1996) 3963, and references therein.